Minimax Robust Landmine Detection Using Forward-Looking Ground-Penetrating Radar

A. D. Pambudi, *Student Member, IEEE,* M. Fauß, *Member, IEEE,* F. Ahmad, *Fellow, IEEE,*
and A. M. Zoubir, *Fellow, IEEE*

Abstract—We propose a robust likelihood-ratio test (LRT) to detect landmines and unexploded ordnance using a forward-looking ground-penetrating radar. Instead of modeling the distributions of the target and clutter returns with parametric families, we construct a band of feasible probability densities under each hypothesis. The LRT is then devised based on the least favorable densities within the bands. This detector is designed to maximize the worst-case performance over all feasible density pairs and, hence, does not require strong assumptions about the clutter and noise distributions. The proposed technique is evaluated using electromagnetic field simulation data of shallow-buried targets. We show that, compared to detectors based on parametric models, robust detectors can lead to significantly reduced false alarm rates, particularly in cases where there is a mismatch between the assumed model and the true distributions.

Index Terms—Landmine detection, forward-looking ground-penetrating radar, likelihood-ratio test, density band model, robust statistic, minimax risk.

I. INTRODUCTION

LANDMINE Monitor 2018 has reported over $122\,000$ civilian casualties and injuries, caused by landmines and other unexploded ordnance (UXO), since it began global tracking in 1999 [1]. It is inevitable that many more occurrences went unrecorded due to the lack of national monitoring systems in some affected countries. UXOs not only pose a threat to the lives and well-being of the population, but also hinder the economic development of a nation. Consequently, further improvements in techniques for reliable and safe detection of UXOs are of critical importance.

A. D. Pambudi is with the Signal Processing Group, Department of Electrical Engineering and Information Technology, Technische Universität Darmstadt, Darmstadt 64283, Germany, and also with the School of Electrical Engineering, Telkom University, Bandung 40257, Indonesia (on extended leave) (e-mail: apambudi@spg.tu-darmstadt.de; apambudi@telkomuniversity.ac.id).

M. Fauß, and A. M. Zoubir are with the Signal Processing Group, Department of Electrical Engineering and Information Technology, Technische Universität Darmstadt, Darmstadt 64283, Germany (e-mail: {mfauss, zoubir}@spg.tu-darmstadt.de).

F. Ahmad is with the Department of Electrical and Computer Engineering, Temple University, Philadelphia, PA 19122, USA (e-mail: fauzia.ahmad@temple.edu).

Ground-Penetrating Radar (GPR) is a nondestructive method that uses electromagnetic radiation to detect buried targets [2], [3]. It can detect metallic as well as non-metallic targets having dielectric properties different from the background medium. A forward-looking GPR (FL-GPR) offers the potential of detecting landmines and UXOs with reduced risk to the operator [4]–[7]. This is accomplished with a large standoff distance between the detector and the targets, rendering it an attractive option compared to a conventional downward-looking radar that incurs the chance of disturbing the scene and activating the targets. However, a challenge of using FL-GPR is that the illuminating signals and the reflected signals experience substantial attenuation owing to the near cancellation of the direct and ground-reflected waves. Furthermore, the interface roughness and subsurface clutter, which are usually highly non-stationary, have a strong impact on FL-GPR performance. In order to reduce detection errors, these effects need to be compensated with an appropriate signal processing method.

Several methods to overcome the challenges of FL-GPR have been proposed [6]–[13]. In [8], the authors consider the problem of detecting buried plastic landmines using FL-GPR and characterize the scattering phenomenon in the time-frequency domain. This motivated the use of a wavelet packet transform and a neural network classifier in [9] to increase the detection performance. By dividing a full frequency band into several sub-bands and employing a multi-feature classifier, improved performance for detecting metallic landmines is achieved in [10]. In [11], an adaptive multi-transceiver imaging technique is proposed that effectively integrates imaging information obtained through platform motion. Feature extraction of the bistatic scattering images from a multiple-input-multiple-output radar system is proposed in [12] to differentiate targets from clutter. A time-reversal imaging algorithm is proposed in [13], which employs three-dimensional finite-difference time-domain modeling to characterize the scattering from the ground surface and buried targets. The method proposed in [6] forms a multiview tomographic image as a reference for performing a statistical parametric test to detect shallow-buried landmines in the presence of a rough ground surface. Furthermore, an adaptive approach is proposed in [7] to reduce the false alarm rate by iteratively updating the estimated parameters of the clutter and target distributions under changing viewpoints. Another adaptive method for estimating the statistics of parameters with application to detecting objects in through-the-wall imaging can be found in [14] [15].

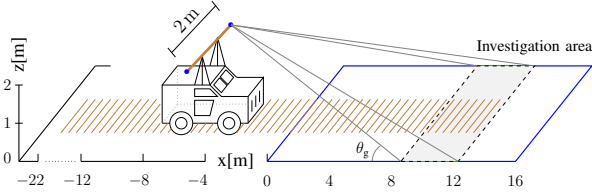In this paper, we propose a pixel-wise likelihood-ratio test

Fig. 1: FL-GPR vehicle-based system with antenna array mounted on top. Brown lines on the ground indicate sensor array positions.

TABLE I: List of targets and their types.

No.	Mine type	No.	Mine type
{1}	Metallic anti-personnel	{4,5}	Metallic anti-tank
{2,8}	Plastic anti-personnel	{9}	Plastic anti-tank
{3,6,7}	Metallic 155mm shell		

(LRT) to detect landmines and UXOs in the image domain. In contrast to existing approaches, we design the test to be robust against statistical model deviations [16]. More precisely, instead of modeling the distributions of the pixel intensity under each hypothesis with a parametric family of distributions, we use training data to construct two feasible bands within which the probability density functions (pdfs) under either hypothesis are assumed to lie. The detector is then designed such that it minimizes the maximum error probability for all possible density pairs within the two bands. In [17]–[20], it is shown that under very mild assumptions a minimax optimal test for such an uncertainty model is guaranteed to exist. The reason behind following a minimax approach is that accurate estimation of the distribution of the background clutter, given its non-stationary behavior, is highly challenging. The proposed technique overcomes this issue since it does not need an accurate estimate in the first place and is guaranteed to perform well over a set of feasible distributions.

The remainder of this paper is organized as follows. Section II describes the configuration of the FL-GPR system and the measurement setup. Section III formulates the target detection problem as a statistical hypothesis test and discusses the differences between the parametric LRT previously studied in [6], [7], [15] and the proposed minimax approach. It also addresses the question of how to construct the least favorable densities (LFD), which play a central role in designing the minimax robust detector. Section IV first discusses how the training data is obtained and how it is used to estimate the target and clutter distributions in existing parametric approaches. Based on these results, two approaches for constructing the uncertainty sets of feasible distributions for the robust detector are detailed, both being special cases of the density band model. In Section V, numerical results in different rough surface environments are presented and the performance of the proposed detector is compared to that of parametric alternatives. Finally, Section VI concludes the paper.

II. FL-GPR SYSTEM AND MEASUREMENT CONFIGURATION

We work with numerical data simulated using the Near-Field Finite-Difference Time-Domain software package, NAFDTD, developed by the U.S. Army Research Laboratory (ARL) [4]. Fig. 1 illustrates the FL-GPR system with a $2\,\mathrm{m}$ wide antenna array, comprising 2 transmitters and 16 receivers, mounted on top of a vehicle at the approximate height of $2\,\mathrm{m}$. In order to sense the investigation area ($16\,\mathrm{m} \times 10\,\mathrm{m}$ blue

rectangle in Fig. 1), the radar platform moves along the x-direction, starting at $-22\,\mathrm{m}$. The FL-GPR system operates in forward-looking mode from $x = -22\,\mathrm{m}$ to $x = 11\,\mathrm{m}$, sensing the investigation area at grazing angle $\theta_\mathrm{g} \in [5°, 20°]$ approximately with a stepped frequency signal covering the $0.3 - 1.5\,\mathrm{GHz}$ band in $6\,\mathrm{MHz}$ increments.

Fig. 2 depicts the measurement configuration considered in the simulation. The investigation area is a rough surface environment containing nine targets. The types of targets are detailed in Table I. Six targets are buried at a depth of 3 cm, five of which are metallic landmines {1, 3, 4, 6, 7} and one is made of plastic {9}. The remaining targets, two plastic landmines {2 and 8} and a metallic one {5}, are placed on the surface. The considered on-surface and shallow-buried target deployments mimic realistic scenarios, typical of anti-personnel landmines and/or anti-tank landmines laid by specialized minelayer vehicles [21]. Plastic landmines are characterized with a relative dielectric constant $\varepsilon_r = 3.1$ and conductivity $\sigma = 2\,\mathrm{mS/m}$, which is representative of a minimum-metallic mine [22]. The ground is modeled as a dielectric medium which is non-dispersive, non-magnetic, and homogeneous with $\varepsilon_r = 6$ and $\sigma = 10\,\mathrm{mS/m}$. These electrical properties are typical of medium-dry soil [23]. The surface roughness is described as a two-dimensional Gaussian random process parameterized by the root mean square height h_{rms} and the correlation length l_c [6]. Here, we consider two surface roughness profiles: ($h_{rms} = 0.8\,\mathrm{cm}$, $l_c = 14.26\,\mathrm{cm}$) and ($h_{rms} = 1.6\,\mathrm{cm}$, $l_c = 14.93\,\mathrm{cm}$).

A total of 90 array positions spaced $\Delta\mathrm{x} = 0.33\,\mathrm{m}$ apart are considered, whose projections on the x-y plane are depicted as parallel brown lines in Fig. 2. Two adjacent array positions realize a full aperture measurement. In each array position, we activate only one transmit element, while all receive elements simultaneously record the reflected signals from the scene. A tomographic image is constructed by coherently integrating multiple full aperture measurements. The tomographic image is composed of four image segments, each of dimension $4\,\mathrm{m} \times 10\,\mathrm{m}$. By integrating eight full aperture measurements with each pair separated by four array positions, we obtain an image segment. Fig. 2 indicates the eight full aperture measurements between -19.33 and $-5\,\mathrm{m}$ used to image the first segment (dashed rectangle in Fig. 2). The full aperture measurements used to construct the second, third, and fourth image segments range from -15.33 to $-1\,\mathrm{m}$, -11.33 to $3\,\mathrm{m}$, and -7.33 to $7\,\mathrm{m}$, respectively. However, these are not depicted in Fig. 2. A tomographic image is thus constructed by integrating 32 full aperture measurements from x $= -19.33\,\mathrm{m}$ to x $= 7\,\mathrm{m}$. In order to improve the detection performance, we generate ten additional images by successively moving the radar closer to the target area. Compared to the image in Fig. 3 corresponding to the farthest viewpoint, the tomographic
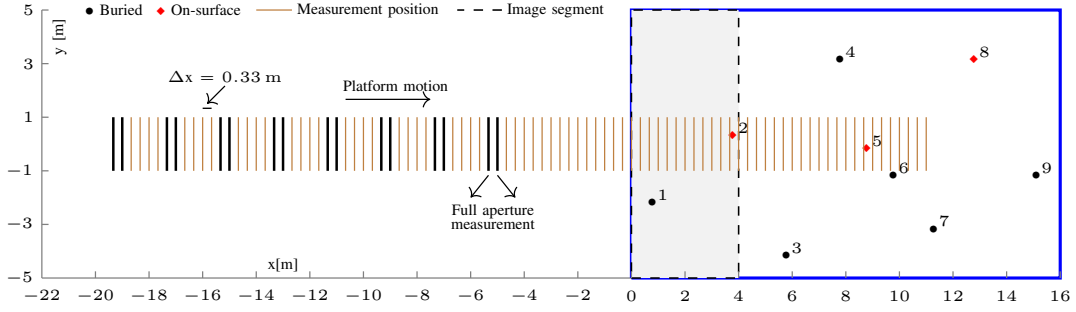
Fig. 2: Top view of the FL-GPR measurement. The blue rectangle indicates the investigation area containing nine targets, buried or placed on ground surface. Eight full aperture measurements are integrated to image the first segment (dashed line rectangle), corresponding to the farthest viewpoint.
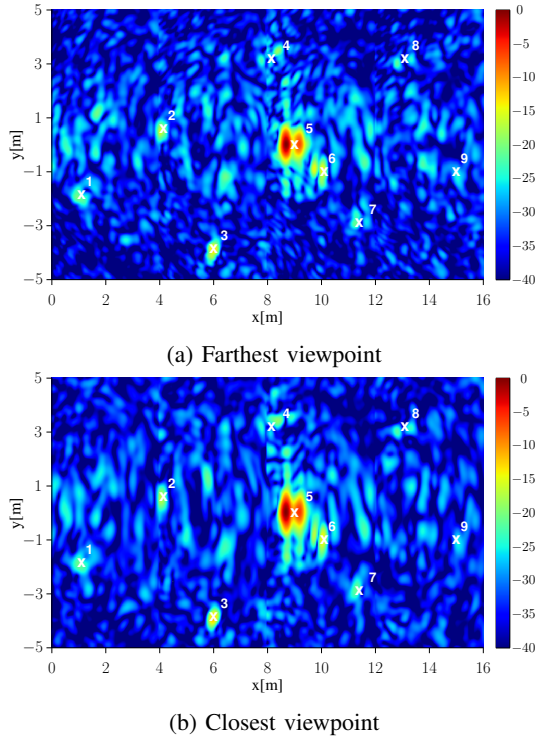

(a) Farthest viewpoint

(b) Closest viewpoint

Fig. 3: Tomographic images for low surface roughness profile ($h_{rms} = 0.8$ cm, $l_c = 14.26$ cm). White crosses indicate targets.

(a) Farthest viewpoint

(b) Closest viewpoint

Fig. 4: Tomographic images for high surface roughness profile ($h_{rms} = 1.6$ cm, $l_c = 14.93$ cm).

image from the viewpoint closest to the scene is realized by integrating measurements from x = −16 m to x = 10.33 m. By this means, we have a total image of $M = 11$ providing various views of the investigation area. For more details of the multiview tomographic imaging approach, refer to [6].

The images in Figs. 3 and 4 are normalized to 40 dB dynamic range and each consists of $N_x = 1153$ pixels in downrange and $N_y = 721$ pixels in crossrange with a resolution of 5 cm. The targets located near the boundaries of the investigation area are less visible since they are outside of the mainlobe of the antenna array whose physical aperture is smaller than the image extent in cross range. Compared to the landmines placed on the surface, the buried landmines are more challenging to discern due to the clutter caused by the radar back-scatter from the rough ground surface. In general,
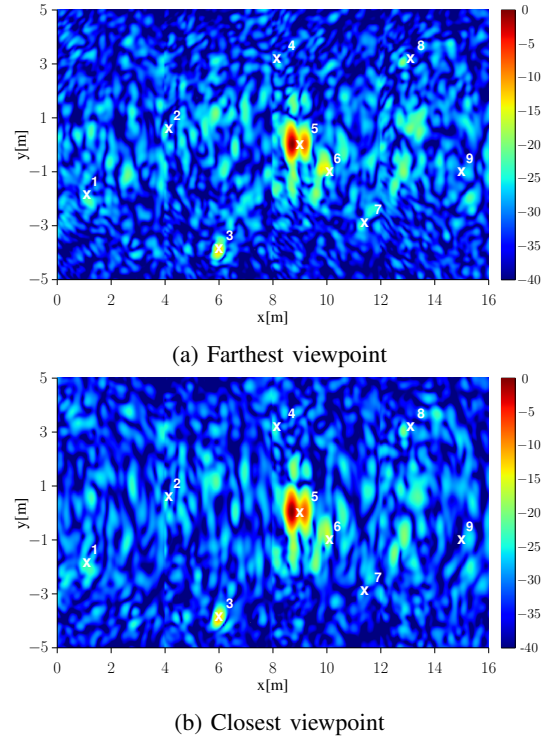
recognizing a plastic landmine is harder than a metallic one, since its return signal energy is comparable to that of clutter. The difference in clutter returns across the different viewpoints is clearly visible and illustrates the non-stationary behavior of the scattering from the rough ground surface. As expected, the higher surface roughness leads to stronger clutter echoes, thus making the detection more challenging.

III. PROBLEM FORMULATION AND THE LIKELIHOOD-RATIO TEST

A tomographic image is represented as a two-dimensional array of normalized pixel intensities

$$x(i,j), \quad 1 \leqslant i \leqslant N_x, \ 1 \leqslant j \leqslant N_y,$$

where $x(i,j) \in [0,1]$. The detection problem is to decide whether a pixel at (i,j) belongs to target or clutter. The problem can be defined as a test between a null and an alternative hypothesis as,

$$
\begin{aligned}
H_0 &: \text{ no target present,} \\
H_1 &: \text{ target present.}
\end{aligned}
\tag{1}
$$

The proposed robust test, as well as the existing parametric LRT [6], [7], which is used as a reference for comparison, are based on the Neyman–Pearson approach [24] to optimal test design. That is, the test is designed such that it minimizes the miss detection (type II error) probability under a constraint on the false alarm (type I error) probability. In other words, it minimizes the probability of confusing a target pixel for a clutter pixel for a given probability of confusing a clutter pixel for a target pixel. In order to highlight the similarities and differences between the parametric and the robust LRT, we briefly summarize the former before detailing the latter.

A. Parametric Likelihood-Ratio Test

For simplicity, let us assume that the pixel intensities of all M tomographic images are independently and identically distributed (iid). For the mth tomographic image, a pixel-wise LRT is given by

$$
L_m(i,j) = \frac{p_1(x_m(i,j))}{p_0(x_m(i,j))} \underset{H_0}{\overset{H_1}{\gtrless}} \gamma,
\tag{2}
$$

where $x_m(i,j)$ denotes the intensity of the pixel at coordinate (i,j) of the mth image and p_s denote the conditional probability density functions of the pixel intensities under hypotheses H_s, $s = 0, 1$. The threshold γ is determined based on the targeted false alarm probability α and can be determined by solving

$$
\alpha = \int_\gamma^\infty f_L(l|H_0)\, \mathrm{d}l
\tag{3}
$$

for γ. Here, $f_L(l\,|\,H_0)$ denotes the density of the likelihood ratio L under the null hypothesis. In [6], [7], the authors show that the pixel intensities approximately follow a Rayleigh distribution under H_0 and a Gaussian mixture distribution under H_1. The corresponding density functions are given by

$$
\begin{aligned}
p_0(x) &= x/\sigma_0^2 \cdot \exp\left(-x/2\sigma_0^2\right), \\
p_1(x) &= \sum_{k=1}^K \phi_k\, \mathcal{N}(x \mid \mu_k, \sigma_k^2),
\end{aligned}
\tag{4}
$$

where σ_0^2 is the parameter of the Rayleigh distribution, $\mathcal{N}(\bullet\,|\,\mu, \sigma^2)$ denotes a Gaussian distribution with mean μ and variance σ^2, K is the number of Gaussian distributions in the mixture, and $\phi_1, \ldots, \phi_K$ are mixture weights. Based on this model, the authors in [6], [7], [25] propose a generalized LRT, i.e., the test statistic in (2) is evaluated by replacing all unknown parameters in (4) with their maximum likelihood estimates.

B. Minimax Robust Likelihood-Ratio Test

The idea of minimax robust hypothesis testing is to design a test such that it works well under all feasible distributions. That is, in contrast to the generalized LRT, which tries to *reduce* the uncertainty by estimating unknown parameters, a minimax robust test *tolerates* uncertainty.

We start by considering the general case of two composite hypotheses

$$
\begin{aligned}
H_0 &: \ P \in \mathcal{F}_0, \\
H_1 &: \ P \in \mathcal{F}_1,
\end{aligned}
\tag{5}
$$

where $\mathcal{F}_0$ and $\mathcal{F}_1$ are two disjoint sets of feasible distributions which are chosen such that they adequately capture the distributional uncertainties of the underlying detection problem. Here, we use Kassam's band model for this purpose, which is a generalization of the ε-contamination model [26] and has been shown to provide a good trade-off between flexibility and tractability [17], [18]. It is given by

$$
\begin{aligned}
\mathcal{F}_0 &= \{p_0 \mid p_0'(x) \leqslant p_0(x) \leqslant p_0''(x)\}, \\
\mathcal{F}_1 &= \{p_1 \mid p_1'(x) \leqslant p_1(x) \leqslant p_1''(x)\},
\end{aligned}
\tag{6}
$$

where p_s' and p_s'' denote lower and upper bounds on the true density, respectively. For the problem at hand, the bounds need to be non-negative functions satisfying

$$
\int p_s'(x)\, \mathrm{d}x \leqslant 1 \leqslant \int p_s''(x)\, \mathrm{d}x, \quad s = 0, 1,
\tag{7}
$$

but can otherwise be chosen freely by the test designer.

In principle, a minimax robust test is designed by finding a pair of densities $(g_0, g_1) \in \mathcal{F}_0 \times \mathcal{F}_1$ which is *least favorable* in the sense that it simultaneously maximizes both error probabilities among all feasible densities. If such a pair exists, the corresponding minimax optimal test can be shown to be a threshold test whose test statistic is the likelihood ratio of the least favorable densities (LFDs) [18], [26]. In [18], it is shown that the LFDs for the band model can, in general, be written as

$$
\begin{aligned}
g_0(x) &= \min\{p_0''(x),\, \max\{a_0\, g_1(x),\, p_0'(x)\}\}, \\
g_1(x) &= \min\{p_1''(x),\, \max\{a_1\, g_0(x),\, p_1'(x)\}\},
\end{aligned}
\tag{8}
$$

where the two constants a_0 and a_1 have to be calculated such that the LFDs are valid densities, i.e., they integrate to one. Based on the procedure outlined in [18], an iterative algorithm to construct the LFDs is provided in Table II. Starting with an initial guess for the LFDs (g_0^0, g_1^0), the algorithm alternately updates g_0^n and g_1^n by finding a root of

$$
f_s(a; g) = \int \min\{p_s''(x), \max\{a\, g(x), p_s'(x)\}\}\, dx - 1,
\tag{9}
$$

which, for a given density g, is a non-decreasing function of the scalar a. The iteration is terminated once both densities have converged within a tolerance δ.

Note that the likelihood ratio of the least favorable densities, $g_1(x)/g_0(x)$, can take six possible values, namely

$$
\frac{g_1(x)}{g_0(x)} \in \left\{ \frac{p_1'(x)}{p_0'(x)}, \frac{p_1'(x)}{p_0''(x)}, \frac{p_1''(x)}{p_0'(x)}, \frac{p_1''(x)}{p_0''(x)}, a_1, \frac{1}{a_0} \right\}.
\tag{10}
$$

The first four values correspond to regions where g_0 or g_1 coincide with either their lower or their upper bound. Hence,

TABLE II: Algorithm to construct the LFDs

Input: p_0', p_0'', p_1', p_1'', g_0^0, g_1^0, δ
Output: g_0, g_1
1: **repeat**
2: $\quad a_0 \quad$ = root of $f_0(a; g_1^n)$
3: $\quad g_0^{n+1} = \min\{p_0'', \max\{a_0\, g_0^n,\, p_0'\}\}$
4: $\quad a_1 \quad$ = root of $f_1(a; g_0^{n+1})$
5: $\quad g_1^{n+1} = \min\{p_1'', \max\{a_1\, g_0^{n+1},\, p_1'\}\}$
6: $\quad$ **if** $\|g_0^n - g_0^{n+1}\| < \delta$ and $\|g_1^n - g_1^{n+1}\| < \delta$
7: $\qquad$ **return** g_0^n, g_1^n
8: $\quad g_0^n = g_0^{n+1}$
9: $\quad g_1^n = g_1^{n+1}$

Fig. 5: Training image T. Normalized tomographic image of the closest viewpoint on flat ground surface.

for the two remaining cases it holds that either $p_1'(x) < g_1(x) < p_1''(x)$, which by (8) implies that

$$g_1(x) = a_1\, g_0(x) \quad \Rightarrow \quad \frac{g_1(x)}{g_0(x)} = a_1, \qquad (11)$$

or that $p_0'(x) < g_0(x) < p_0''(x)$, which implies

$$g_0(x) = a_0\, g_1(x) \quad \Rightarrow \frac{g_1(x)}{g_0(x)} = \frac{1}{a_0}. \qquad (12)$$

We can obtain an interesting special case of the band model by letting $p_0'', p_1'' \to \infty$, so that the LFDs in (8) reduce to

$$\begin{aligned} g_0(x) &= \max\{a_0\, g_1(x),\, p_0'(x)\}, \\ g_1(x) &= \max\{a_1\, g_0(x),\, p_1'(x)\}, \end{aligned} \qquad (13)$$

and the possible values of the likelihood ratio become

$$\frac{g_1(x)}{g_0(x)} \in \left\{ \frac{p_1'(x)}{p_0'(x)},\, a_1,\, \frac{1}{a_0} \right\}. \qquad (14)$$

That is, the density band model reduces to the ε-contamination model, and the corresponding minimax optimal test becomes Huber's clipped likelihood-ratio test, which is robust against outliers [26].

IV. CONSTRUCTION OF THE UNCERTAINTY SETS

Having calculated the LFDs, the robust LRT is then of the form (2), with the parametric densities (p_0, p_1) replaced by the LFDs (g_0, g_1). First, however, the uncertainty sets $\mathcal{F}_0$ and $\mathcal{F}_1$ need to be constructed. In order to do so, we propose a hybrid approach that combines parametric density estimates constructed from training data with classic nonparametric uncertainty models, which is detailed in this section.

A. Training Data

In order to perform the LRT, *a priori* knowledge about the distribution of the pixel intensities under each hypothesis is needed. In order to obtain this knowledge, we use two training images, T and C, generated by the NAFDTD software. The image T is a clutter-free image as shown in Fig. 5, which is a normalized tomographic image that was generated with the same simulation parameters as described in Section II, except that the ground was assumed to be flat. We then employ a region growing algorithm [27], [28] to locate the target pixel regions. First, the center points of the nine target positions are chosen man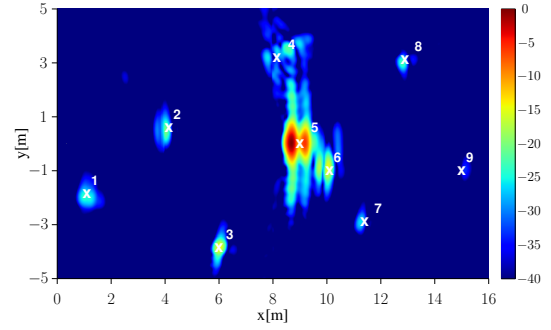ually. The algorithm then successively adds adjacent pixels to the target region based on the connection criterion $\varphi \pm 3\,\mathrm{dB}$, where φ denotes the pixel intensity of the seed points; see [27], [28] for more details. The output of the region growing algorithm is a binary mask given by

$$\mathrm{BM}(i,j) = \begin{cases} 1, & \text{target region at } (i,j), \\ 0, & \text{non-target region at } (i,j), \end{cases} \qquad (15)$$

with $i = 1, ..., N_\mathrm{x}$ and $j = 1, ..., N_\mathrm{y}$. By multiplying the original image T with the mask BM, we obtain the image $\boldsymbol{T} = T \cdot \mathrm{BM}$ that only contains the target pixels and zeros.

The training image C is the closest viewpoint tomographic image for the low surface roughness profile ($h_\mathrm{rms} = 0.8\,\mathrm{cm}$, $l_c = 14.26\,\mathrm{cm}$) as shown in Fig. 3b. The image C is multiplied by the mask image complement BM^c to obtain the image $\boldsymbol{C}$, which is composed of only clutter pixels and zeros. In this way, we obtain two data sets, $\mathcal{X}_t$ and $\mathcal{X}_c$, containing only target and clutter pixels, respectively:

$$\begin{aligned} \mathcal{X}_t &= \{\, x \,|\, x \in \boldsymbol{T},\, x > 0 \,\}, \\ \mathcal{X}_c &= \{\, x \,|\, x \in \boldsymbol{C},\, x > 0 \,\}. \end{aligned} \qquad (16)$$

The data set $\mathcal{X}_t$ consists of $N_t = 3206$ pixels, while the total pixels in set $\mathcal{X}_c$ equals $N_c = N_\mathrm{xy} - N_t$, where $N_\mathrm{xy} = N_\mathrm{x} \times N_\mathrm{y}$. In the next section, we detail how the uncertainty set needed for the robust likelihood-ratio test is constructed from these training data sets.

The histograms of the training data sets $\mathcal{X}_c$ and $\mathcal{X}_t$ are shown in Fig. 6. As mentioned in Section III, the authors of [6], [15], [29] showed that the clutter pixels are approximately Rayleigh distributed, while the distributions of the target pixels can be approximated by a Gaussian mixture distribution. Our aim is to design the robust test such that, on one hand, prior knowledge of the shape of the distributions can still be incorporated, but on the other hand, it is insensitive to deviations from the assumed model. This is accomplished by using the parametric distributions proposed in [6], [15], [29] as *nominal distributions* around which a neighborhood of feasible distributions is constructed. The robust detector is then designed such that it is minimax optimal over the set of feasible distributions. Two ways of choosing the neighborhood are detailed below: the density band model and the ε-contamination model.
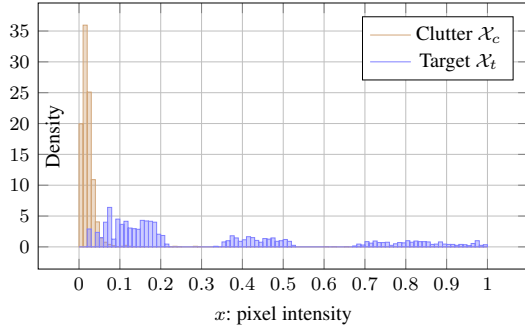
Fig. 6: Histogram of the training data sets $\mathcal{X}_c$ and $\mathcal{X}_t$.

TABLE III: The parameter estimates for p_0, p_1.

$\hat{\sigma}_0$	$\hat{\sigma}_1$	$\hat{\sigma}_2$	$\hat{\sigma}_3$	$\hat{\phi}_1$
0.025	0.050	0.048	0.088	0.601

$\hat{\phi}_2$	$\hat{\phi}_3$	$\hat{\mu}_1$	$\hat{\mu}_2$	$\hat{\mu}_3$
0.212	0.186	0.117	0.430	0.833

B. Density Band Model

For the first uncertainty model, we construct a band of feasible densities as defined in (6). More precisely, the lower and upper bounds are chosen as

$$p'_s(x) = 0.8\, p_s(x), \quad p''_s(x) = 2.5\, p_s(x), \quad s = 0, 1, \quad (17)$$

where p_0 and p_1 denote the parametric density estimates in (4). That is, we assume that the true distributions are close to the nominal distributions in the sense that the probability mass on any measurable set $E \subset \mathbb{R}$ is lower bounded by $0.8\, P_s(E)$ and upper bounded by $2.5\, P_s(E)$. Note that this implies that the deviations from the nominal model are continuous, i.e., events that are highly (un)likely under the nominal distribution are also highly (un)likely under all feasible distributions. The particular values of 0.8 and 2.5 were chosen heuristically based on a series of experiments. More specifically, they have been shown to correspond to a good compromise between guarding against slight but systematic model mismatches and guarding against severe but rare outliers [18], [19].

Using the training data detailed above, we obtained maximum likelihood estimates for the parameters of the densities in (4) as shown in Table III. The corresponding bands of feasible densities are shown in Fig. 7a, indicated by the shaded areas. Fig. 7a also depicts the LFDs for this model, g_0 and g_1. The latter were calculated using the iterative algorithms detailed in Section III, using the nominal densities p_0 and p_1 as starting points. The tolerance was set to $\delta = 0.001$. By inspection, each LFD coincides with its upper or lower bound on certain intervals. Moreover, according to (10), it holds that
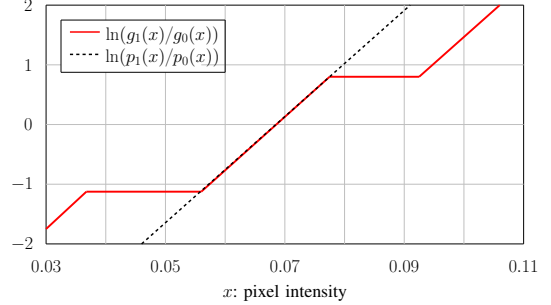
$$\frac{g_1(x)}{g_0(x)} \in \left\{ \frac{p_1(x)}{p_0(x)}, \frac{8}{25}\frac{p_1(x)}{p_0(x)}, \frac{25}{8}\frac{p_1(x)}{p_0(x)}, a_1, \frac{1}{a_0} \right\}. \quad (18)$$

That is, the robust likelihood ratio is a scaled or clipped version of the nominal likelihood ratio.

In Fig. 7b, the robust likelihood ratio is plotted in logarithmic scale. The two clipping constants are obtained as $\ln a_1 = -1.125$ and $\ln a_0 = -0.8$ and are attained on the
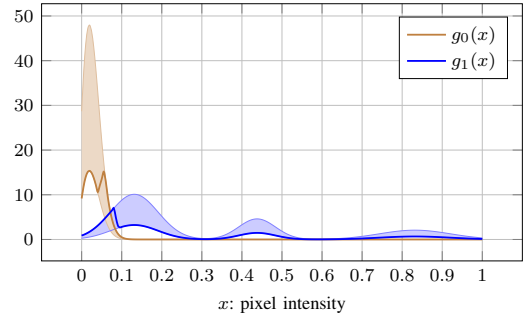
(a) Density band model and LFDs

(b) Likelihood ratio

Fig. 7: Density band model in (17) with corresponding LFDs and their likelihood ratio in logarithmic scale.

intervals $0.0367 \leqslant x \leqslant 0.0560$ and $0.0775 \leqslant x \leqslant 0.0925$, respectively. In the other ranges, the minimax test statistic is either the same as that of the parametric test (dashed line) or a scaled version.
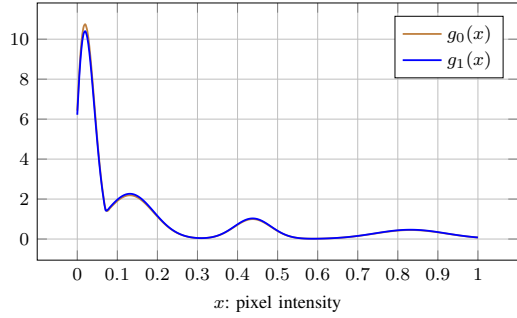
C. Outlier Model

For the second uncertainty model, we assume that the true distributions are close to the nominal ones in the sense that, under each hypothesis, a majority of the pixels is distributed according to the nominal model, whereas a fraction of ε are allowed to be distributed arbitrarily. This is the classic outlier model first studied by Huber [26]. For the examples in this section, we assumed a contamination ratio of $40\,\%$, i.e.,

$$p'_s(x) = 0.6\, p_s(x), \quad p''_s(x) = \infty, \quad s = 0, 1. \quad (19)$$

This contamination ratio has been identified as a minimum value such that $g_0(x) \neq g_1(x)$, that is, the least favorable densities do not overlap completely. This value was also investigated for the outlier model in [19]. On the one hand, the assumption that only $60\,\%$ of the pixels follow the nominal model is rather pessimistic. On the other hand, it is well in line with the idea of minimax robustness, i.e., preparing for the worst case.

Fig. 8a shows the LFDs for the uncertainty model in (17). Note that they are difficult to distinguish by inspection since they are most similar by construction. As stated in (14) and shown in Fig. 8b, the corresponding robust likelihood ratio in logarithmic scale satisfies

$$\ln \frac{g_1(x)}{g_0(x)} \in \left\{ \ln \frac{p_1(x)}{p_0(x)}, -0.205, 0.241 \right\}. \quad (20)$$

(a) LFDs of the outlier model
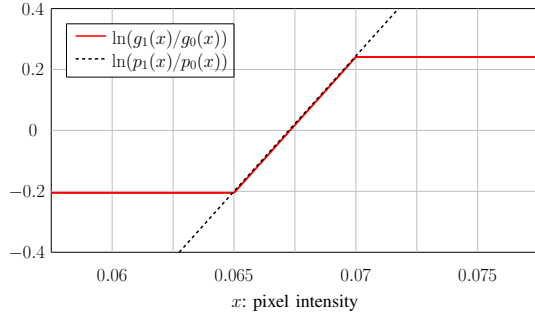
(b) Likelihood ratio

Fig. 8: LFDs of the outlier model in (19) and their likelihood ratio in logarithmic scale.

That is, it coincides with the nominal likelihood ratio on the interval $0.065 \leqslant x \leqslant 0.07$ and is clipped at either -0.205 or 0.241 everywhere else. This clipping ensures that the influence of x is limited and trusted only up to a certain level and illustrates a key feature of robust detectors, namely that a few outlying observations should not be able to outweigh the majority of the data.

V. Simulation Results

Multiple tomographic images obtained from different viewpoints, as described in Section II, are used for the detection. More precisely, first, the LRT is performed on each image, then the resulting binary masks are multiplied pixel-by-pixel. That is, the final target regions are given by the intersections of the target regions of the individual images. This fusion rule is also known as *hard fusion* in the literature. For both the nominal and the robust test the likelihood ratio threshold γ in (2) is obtained by solving (3) for the estimated nominal and least favorable distributions, respectively.

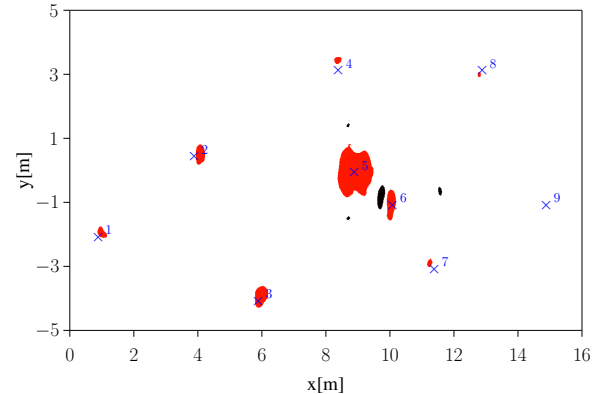### A. Detection Results in Low Surface Roughness Environments

The binary image resulting from the parametric LRT is shown in Fig. 9a for a targeted false alarm rate of $\alpha = 0.05$. The blue crosses indicate the central position of the true targets. White pixels indicate a correct decision for H_0 (no target present), red pixels indicate a correct decision for H_1 (target present), and black pixels indicate an erroneous decision for H_1 (false alarm). As can be seen, all nine targets are successfully detected, but there are several false alarms as well. The large red area at $9\,\mathrm{m}$ downrange is due to the
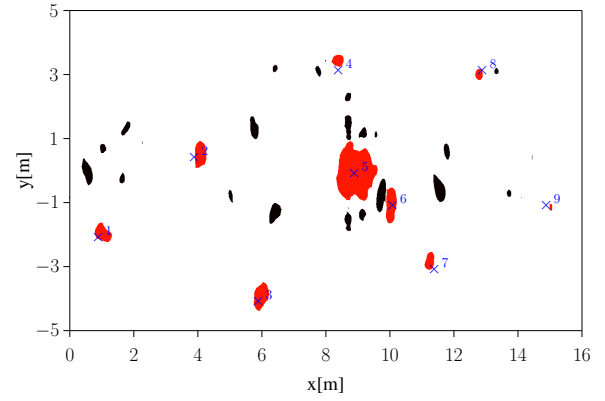
(a) Parametric LRT
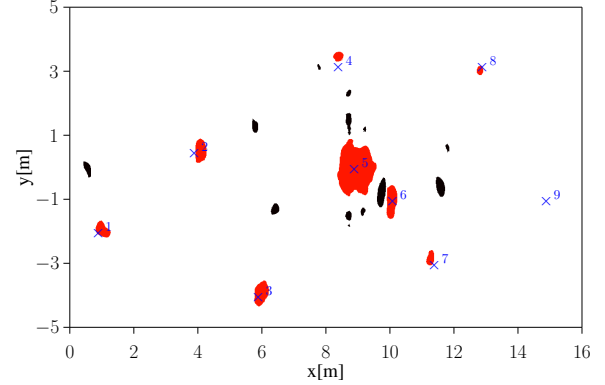
(b) Robust LRT using density band model

(c) Robust LRT using outlier model

Fig. 9: Detection results for $\alpha = 0.05$ in low surface roughness environments. Color coding: detected targets (red), false alarms (black).

strong reflection from the metallic AT landmine placed on the surface.

Fig. 9b depicts the result of the minimax LRT based on the density band model. Here, the number of false alarms is reduced significantly at the cost of one missing target, which is a buried plastic AT landmine located at the farthest downrange. This result is to be expected: Since the robust detector uses much weaker assumptions about the clutter distribution, it is less likely to confuse strong clutter echoes for targets. On the downside, this also makes the detector less sensitive towards weak target echoes.

(a) Parametric LRT

(b) Robust LRT using density band model
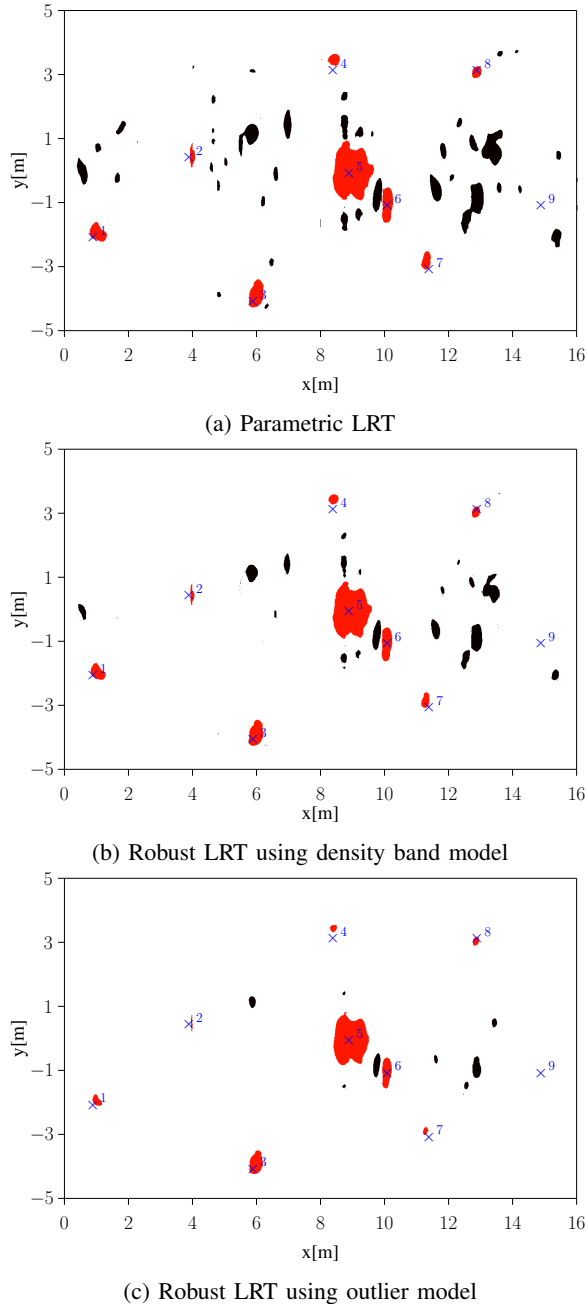

(c) Robust LRT using outlier model

Fig. 10: Detection results for $\alpha = 0.05$ in mixed surface roughness environments. Color coding: detected targets (red), false alarms (black).

It should be highlighted that the detectors whose results are shown in Fig. 9a and Fig. 9b are both designed under the same false alarm constraint.[1] Moreover, the effect of using least favorable distributions is distinctly different from simply increasing the detection threshold of the parametric test. This can be seen from the fact that the target regions for all detected landmines are approximately of the same size. Increasing the threshold of the nominal test would also reduce the number

[1]Determining whether or not the targeted false alarm rate is met is non-trivial since the binary images also depend on the region growing algorithm, whose effects are not taken into account in the design of the detector.

of false alarms, but at the cost of significantly smaller target regions.

This effect can indeed be observed in Fig. 9c, where the detection results of the minimax detector based on the second uncertainty model, the outlier model in (17), are depicted. The outlier model allows for significantly more uncertainty than the band model so that it is even less sensitive to clutter, while still correctly detecting all targets except for the plastic landmine 9. Hence, in this examples the outlier model can be argued to yield the best results. However, one should note that under the larger uncertainty model, the correctly detected targets are starting to be affected in the sense that the corresponding target regions are noticeably smaller and some landmines are "almost" missed. Given the grave consequences of having missed a target, this trade-off needs to be kept in mind when designing robust tests for landmine detection.

B. Detection Results in Mixed Surface Roughness Environments

A main advantage of minimax robust detectors is that they work well under various conditions, without having to estimate the corresponding parameters. However, this also implies that robust detectors do not adapt to the observed data. Consequently, the advantages of robust detectors should be most pronounced in scenarios where adapting to the environment is difficult, i.e., the true distributions cannot reliably be estimated from the available training data. In FL-GPR, such situations occur when the statistical properties of the clutter are different for each measurement. This can happen, for example, in environments where the surface roughness of the ground changes frequently.

In order to simulate such a scenario, the region of interest shown in Fig. 2 is divided into four areas whose roughness alternates between the low and the high profile. Each area has a size of $4\,\text{m} \times 10\,\text{m}$. Areas in the downrange from $4\,\text{m}$ to $8\,\text{m}$ and from $12\,\text{m}$ to $16\,\text{m}$ admit a high roughness profile ($h_{rms} = 1.6\,\text{cm}$, $l_c = 14.93\,\text{cm}$), while the remaining areas admit the low roughness profile ($h_{rms} = 0.8\,\text{cm}$, $l_c = 14.26\,\text{cm}$) that was used to generate the training data. The tomographic image for the higher roughness profile is shown in Fig. 4. The detection results for this scenario are shown in Fig. 10. All detectors generally exhibit an increased number of errors, especially on the segments of high roughness. However, it can be seen that the robust tests are significantly less affected by the changing clutter properties. Especially the one based on the outlier uncertainty model manages to keep the number of false alarms in check, without increasing the number of missed targets.

C. Detection Results in High Surface Roughness Environments

Finally, we consider a scenario where the entire investigation area admits a high roughness profile. Fig. 11 shows the detection results for this scenario. Each detector commonly presents three missing targets, which are buried landmines number 4 and 9, and shell number 7. The increased number of errors is to be expected since this is an effect of a mismatch

TABLE IV: Number of false alarms (FA) and number of missed detections (MD) for different surface roughness.

LRT detector	Low		Mixed		High	
	FA	MD	FA	MD	FA	MD
Parametric model	22	0	40	1	41	3
Robust (band model)	12	1	19	1	17	3
Robust (outlier model)	4	1	8	1	12	3

condition between the true distribution of the measurement and the assumed model. However, in comparison to the parametric model, the robust detectors are preferable with fewer false alarms.

This detection performance can be improved by carefully assigning the band interval which naturally aligns with the non-stationary behavior of the measurements [30], [31]. A different approach can also be applied by considering the LRT which takes into account statistical dependencies between measurements [32]. These methods are currently being explored and for a separate publication. The robust LRT using the

Table IV summarizes the performance of each detector in different rough surface environments. Accommodating uncertainties in the distribution with the robust LRTs reduces the number of false alarms significantly for all surface roughness levels. The robust LRT using the outlier model is preferable with only one missed detection for both low and mixed roughness profiles, with the lowest number of false alarms among all detectors.

VI. Conclusion

We have investigated the problem of detecting landmines and unexploded ordnance in a rough surface environment using Forward-Looking Ground-Penetrating Radar. A minimax robust likelihood-ratio test has been designed by constructing a density band under each hypothesis and then finding the corresponding least favorable densities. The detection performance of the proposed robust detector has been evaluated using electromagnetic modeled data for different surface roughness and has been compared to alternative parametric approaches. Robust detectors have been shown to significantly reduce the false alarm rate while maintaining a comparable detection rate. However, it has also been shown that the uncertainty model needs to be chosen carefully in order to avoid potential over-robustification. All in all, robust hypothesis testing is a promising method to improve the accuracy of GPR landmine detectors that has not been sufficiently explored yet. In particular, the question of how uncertainty sets can be constructed in a data-driven manner certainly warrants further research.

Acknowledgment

References

[1] M. Committee, *Landmine Monitor 2018.* International Campaign to Ban Landmines–Cluster Munition Coalition (ICBL-CMC), Nov. 2018.

(a) Parametric LRT

(b) Robust LRT using density band model

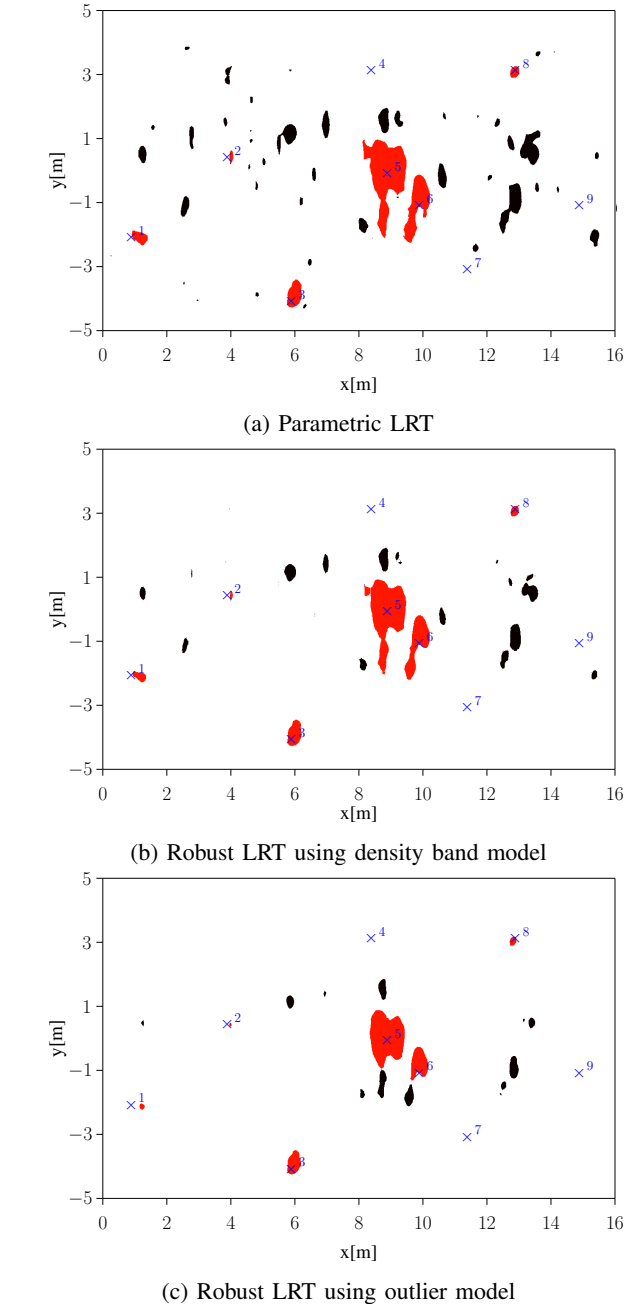(c) Robust LRT using outlier model

Fig. 11: Detection results for $\alpha = 0.05$ in high surface roughness environments. Color coding: detected targets (red), false alarms (black).

[2] D. J. Daniels, "Surface-penetrating radar," *Electron. Commun. Eng. J.*, vol. 8, no. 4, pp. 165–182, Aug. 1996.
[3] A. M. Zoubir, I. Chant, C. Brown, B. Barkat, and C. Abeynayake, "Signal processing techniques for landmine detection using impulse ground penetrating radar," *IEEE Sensors J.*, vol. 2, no. 1, pp. 41–51, Feb. 2002.
[4] T. Dogaru, "NAFDTD–a near-field finite difference time domain solver," U.S. Army Research Laboratory, Final ARL-TR-6110, Sep. 2012.
[5] B. R. Phelan, M. A. Ressler, G. J. Mazzaro, K. D. Sherbondy, and R. M. Narayanan, "Design of spectrally versatile forward-looking ground-penetrating radar for detection of concealed targets," in *Proc. SPIE-Int. Soc. Opt. Eng.*, 2013, p. 87140B.
[6] D. Comite, F. Ahmad, T. Dogaru, and M. G. Amin, "Multiview imaging for low-signature target detection in rough-surface clutter environment," *IEEE Trans. Geosci. Remote Sens.*, vol. 55, no. 9, pp. 5220–5229, Sep.

2017.

[7] D. Comite, F. Ahmad, T. Dogaru, and M. G. Amin, "Adaptive detection of low-signature targets in forward-looking GPR imagery," *IEEE Geosci. Remote Sens. Lett.*, pp. 1520–1524, Oct. 2018.

[8] Y. Sun and J. Li, "Time–frequency analysis for plastic landmine detection via forward-looking ground penetrating radar," *IEE Proc. Radar, Sonar, Nav.*, vol. 150, no. 4, pp. 253–261, Nov. 2003.

[9] Y. Sun and J. Li, "Adaptive learning approach to landmine detection," *IEEE Trans. Aerosp. Electron. Syst.*, vol. 41, no. 3, pp. 973–985, Jul. 2005.

[10] T. Wang, J. M. Keller, P. D. Gader, and O. Sjahputera, "Frequency subband processing and feature analysis of forward-looking ground-penetrating radar signals for land-mine detection," *IEEE Trans. Geosci. Remote Sens.*, vol. 45, no. 3, pp. 718–729, Mar. 2007.

[11] T. Ton, D. Wong, and M. Soumekh, "ALARIC forward-looking ground penetrating radar system with standoff capability," in *Proc. IEEE Int. Conf. Wireless Inf. Technol. Syst.*, 2010, pp. 1–4.

[12] T. Jin, J. Lou, and Z. Zhou, "Extraction of landmine features using a forward-looking ground-penetrating radar with MIMO array," *IEEE Trans. Geosci. Remote Sens.*, vol. 50, no. 10, pp. 4135–4144, Oct. 2012.

[13] D. Liao, T. Dogaru, and A. Sullivan, "Large-scale, full-wave-based emulation of step-frequency forward-looking radar imaging in rough terrain environments," *Sens. Imaging*, vol. 15, no. 1, Apr. 2014.

[14] C. Debes, J. Riedler, A. M. Zoubir, and M. G. Amin, "Adaptive target detection with application to through-the-wall radar imaging," *IEEE Trans. Signal Process.*, vol. 58, no. 11, pp. 5572–5583, Nov. 2010.

[15] C. Debes, M. G. Amin, and A. M. Zoubir, "Target detection in single- and multiple-view through-the-wall radar imaging," *IEEE Trans. Geosci. Remote Sens.*, vol. 47, no. 5, pp. 1349–1361, May 2009.

[16] A. M. Zoubir, V. Koivunen, E. Ollila, and M. Muma, *Robust Statistics for Signal Processing*. Cambridge University Press, 2018.

[17] S. Kassam, "Robust hypothesis testing for bounded classes of probability densities (corresp.)," *IEEE Trans. Inf. Theory*, vol. 27, no. 2, pp. 242–247, Mar. 1981.

[18] M. Fauß and A. M. Zoubir, "Old bands, new tracks—revisiting the band model for robust hypothesis testing," *IEEE Trans. Signal Process.*, vol. 64, no. 22, pp. 5875–5886, Nov. 2016.

[19] A. D. Pambudi, M. Fauß, F. Ahmad, and A. M. Zoubir, "Robust detection for forward-looking GPR in rough-surface clutter environments," in *Proc. IEEE Asilomar Conf. Signals, Syst., Comput.*, 2018, pp. 2077–2080.

[20] A. D. Pambudi, M. Fauß, F. Ahmad, and A. M. Zoubir, "Forward looking GPR-based landmine detection using a robust likelihood ratio test." in *Proc. European Signal Process. Conf.*, 2019.

[21] M. of Defence (MoD), "Ministry of defence annual report and accounts 2013-14," Ministry of Defence United Kingdom, Annual Report HC 764, Nov. 2014.

[22] U. S. GAO, "Military operations: Information on the united states use of land mines in the persian gulf war," United States General Accounting Office (GAO), Annual Report GAO-02-1003, Sep. 2002.

[23] ITU-R, "Electrical characteristics of the surface of the earth," Radio Communication Sector of International Telecommunication Union (ITU-R), Recommendation P. 527-4, Jun. 2017.

[24] E. L. Lehmann and J. P. Romano, *Testing Statistical Hypotheses*. Springer New York, 2005.

[25] C. H. Seng, A. Bouzerdoum, M. G. Amin, and F. Ahmad, "A gaussian-rayleigh mixture modeling approach for through-the-wall radar image segmentation," in *Proc. IEEE Int. Conf. Acoust., Speech, Signal Process.*, 2012, pp. 877–880.

[26] P. J. Huber, "A robust version of the probability ratio test," *Ann. Math. Stat.*, vol. 36, no. 6, pp. 1753–1758, Dec. 1965.

[27] R. Adams and L. Bischof, "Seeded region growing," *IEEE Trans. Pattern Anal. Mach. Intell.*, vol. 16, no. 6, pp. 641–647, Jun. 1994.

[28] L. Rueda, D. Mery, and J. Kittler, Eds., *Progress in Pattern Recognition, Image Analysis and Applications*. Springer-Verlag Berlin Heidelberg, 2007.

[29] D. Liao and T. Dogaru, "Full-wave characterization of rough terrain surface scattering for forward-looking radar applications," *IEEE Trans. Antennas Propag.*, vol. 60, no. 8, pp. 3853–3866, Aug. 2012.

[30] A. D. Pambudi, M. Fauß, and A. M. Zoubir, "Kernel-based cooperative robust sequential hypothesis testing," in *Proc. Int. Conf. Signals Syst.*, 2018, pp. 42–46.

[31] A. M. Zoubir and D. R. Iskander, *Bootstrap Techniques for Signal Processing*. Cambridge University Press, 2004.

[32] S. G. Iyengar, P. K. Varshney, and T. Damarla, "A parametric copula-based framework for hypothesis testing using heterogeneous data," *IEEE Trans. Signal Process.*, vol. 59, no. 5, pp. 2308–2319, May 2011.

Afief D. Pambudi (S'16) is a member of the Signal Processing Group and an associate member of the Graduate School Computational Engineering, Technische Universiät Darmstadt, Germany. Currently, he is working towards the PhD degree under the supervision of Prof. Abdelhak M. Zoubir. His research interests center around topics from signal detection and estimation, robust statistics, and radar signal processing.

Michael Fauß (M'17) received the Dipl.-Ing. degree from Technische Universität München, Germany, in 2010 and the Dr.-Ing. degree from Technische Universität Darmstadt, Germany, in 2016, both in electrical engineering. In November 2011, he joined the Signal Processing Group at Technische Universität Darmstadt and in 2017 he received the dissertation award of the German Information Technology Society for his PhD thesis on robust sequential detection. In September 2019 he joined Prof. H. Vincent Poor's group at Princeton University as a postdoc on a research grant by the German Research Foundation (DFG). His current research interests include statistical robustness, sequential detection and estimation, and the role of similarity measures in statistical inference.

Fauzia Ahmad (F'18) received her Ph.D. degree in electrical engineering from the University of Pennsylvania, Philadelphia, PA, USA, in 1997. Since 2016, she has been with Temple University, Philadelphia, PA, USA, where she is currently an Associate Professor with the Department of Electrical and Computer Engineering. Her research interests include the areas of statistical signal and array processing, computational imaging, compressive sensing, waveform design, target localization and tracking. She has authored over 240 journal articles and peer-reviewed conference papers and eight book chapters in the aforementioned areas. She is a Fellow of the International Society for Optics and Photonics (SPIE). She is a member of the Sensor Array and Multichannel Technical Committee of the IEEE Signal Processing Society, the Computational Imaging Technical Committee of the IEEE Signal Processing Society, the Radar Systems Panel of the IEEE Aerospace and Electronic Systems Society, and the Electrical Cluster of the Franklin Institute Committee on Science and the Arts. She is an Associate Editor of the IEEE TRANSACTIONS ON COMPUTATIONAL IMAGING, and the IEEE TRANSACTIONS ON AEROSPACE AND ELECTRONIC SYSTEMS. She also serves on the editorial board of the IET Radar, Sonar, & Navigation. She is the chair of the IEEE Dennis J. Picard Medal for Radar Technologies and Applications Committee.

Abdelhak M. Zoubir (F'08) received the Dr.-Ing. degree from Ruhr-Universität Bochum, Germany, in 1992. He was with Queensland University of Technology, Australia from 1992 to 1998, where he was an Associate Professor. In 1999, he joined Curtin University of Technology, Australia, as a Professor of telecommunications. In 2003, he moved to Technische Universität Darmstadt, Germany as a Professor of signal processing and the head of the Signal Processing Group. His research interests include statistical methods for signal processing with emphasis on bootstrap techniques, robust detection and estimation and array processing applied to telecommunications, radar, sonar, automotive monitoring and safety, and biomedicine. He published more than 400 journal and conference papers on these areas. He is an IEEE Distinguished Lecturer (Class 2010-2011). He served as a General Chair and Technical Chair of numerous international IEEE conferences. He also served on publication boards of various journals, most notably, he served a three-year term as the Editor-In-Chief of the IEEE Signal Processing Magazine (2012-2014). He was the Chair (2010-2011), a Vice-Chair (2008-2009), and a Member (2002-2007) of the IEEE SPS Technical Committee Signal Processing Theory and Methods (SPTM). He was a Member of the IEEE SPS Technical Committee Sensor Array and Multichannel Signal Processing (SAM) from 2007 until 2012. He also served on the Board of Directors of the European Association of Signal Processing (EURASIP) (2009-2016) and on the Board of Governors of the IEEE SPS (2015-2017). He served as the President of EURASIP from 2017 to 2018.